Therapeutic Targeting of Epithelial–Mesenchymal Cellular Plasticity in Pancreatic Cancer

Eric W. Lin[1,2,3], Priyadarshini Pathak[1,3], Aileen O'Shea[4], Beatrice Awasthi[1,5], Ildiko E. Phillips[1], Joshua R. Kocher[1], Yuhui Song[1], Michael J. Raabe[1], Katherine H. Xu[1], Bidish K. Patel[1], Nicole Lester[1,5], Jung Woo Bae[1,5], M. Lisa Zhang[6], Linda T. Nieman[1], Lawrence S. Blazkowsky[1,3], Elizabeth P. Walsh[1,3], Aparna R. Parikh[1,3], Andrea Hansen[3], Joanna Caufield[3], Gordon Newbert[3], Akwi W. Asombang[2], Brenna Casey[2], Jonah Cohen[2], Brian C. Jacobson[2], Kumar Krishnan[2], Raul Uppot[4], Ralph Weissleder[4], Nora K. Horick[7], William L. Hwang[1,5,8], Mukesh G. Harisinghani[4], David T. Ting[1,3], and Colin D. Weekes[1,3]

ABSTRACT

Purpose: Pancreatic ductal adenocarcinoma (PDAC) cells exist on a spectrum of epithelial (E) and quasi-mesenchymal (QM) transcriptional states, with differences in sensitivity to FOLFIRINOX (FFX). Glycogen synthase kinase 3β (GSK-3β) is a key regulator of PDAC cell epithelial-to-mesenchymal transition (EMT).

Patients and Methods: *In vitro* analysis of PDAC cell lines combined with multiomic analysis of data from a GSK-3β inhibitor trial (NCT05077800) was conducted to evaluate treatment effects on EMT.

Results: GSK-3β inhibition with elraglusib (ELRA) drives QM PDAC cells toward an E state, demarcated by decreased transcription of QM genes *FN1* and *TGFB1* and an induction of E genes *KRT8* and *CEACAM6*. A comparison of differentially expressed genes (DEG) in PDAC cell lines with tumors from patients with PDAC treated in a safety cohort combining FFX, ELRA, and losartan demonstrated 97 overlapping DEGs with concordant directional changes. ELRA treatment consistently suppressed EMT pathway expression. The synergy of ELRA with cytotoxic doses of FFX in 3D culture was observed only in QM PDAC lines. The FFX/ELRA combination demonstrated initial evidence of clinical benefit, with three of six patients experiencing a partial response (PR) for a duration of at least 20 months. Interestingly, PRs were observed in patients with tumors demonstrating a baseline high proportion of QM cells that transitioned to E predominant tumors with ELRA treatment. Lastly, the influx of M1 tumor-associated macrophages, CD4/CD8 lymphocytes, and NK cells was observed with ELRA clinical response using a combination of GeoMx, snRNA-seq, and ferumoxytol-enhanced MRI.

Conclusions: GSK-3β blockade synergizes with FFX by modulating PDAC plasticity while promoting the development of a tumor-suppressive immune microenvironment.

Introduction

Pancreatic ductal adenocarcinoma (PDAC) remains a recalcitrant disease with a 5-year survival rate of 13%. Combination cytotoxic chemotherapy was originally demonstrated to benefit patients with metastatic disease over a decade ago, with FOLFIRINOX [FFX; 5-fluorouracil (5-FU), oxaliplatin, and irinotecan] in 2011 (1) and gemcitabine combined with nab-paclitaxel in 2013 (2). These combination therapies both have response rates around 30% with generally nonoverlapping effects in patients with PDAC.

A series of genomic and transcriptomic studies has resulted in the classification of PDAC cells into two specific transcriptional subtypes: a classical epithelial (E) subtype and a quasi-mesenchymal (QM; also known as basal or squamous) subtype (3–6). The COMPASS trial provided initial evidence of the clinical importance of these transcriptional subtypes as predictive therapeutic biomarkers. Specifically, this study demonstrated that in patients with locally advanced and metastatic PDAC, the expression of the E cell transcription factor GATA6—associated with the E phenotype—resulted in improved progression-free survival (PFS) in response to first-line FOLFIRINOX compared with patients with QM-predominant tumors (7, 8). Similarly, our prior work has demonstrated that FOLFIRINOX treatment of PDAC cells induces epithelial-to-mesenchymal transition (EMT), leading to the enrichment of QM phenotype persister PDAC cell populations in preclinical models and neoadjuvant FOLFIRINOX-treated PDAC tumors (9, 10). Although there are some genomic features that track with these transcriptional phenotypes, including *SMAD4* loss (11) and *KRAS* or *GATA6* copy-number gain (12), E and QM states are driven primarily by a combination of epigenetic changes—mediated by tumor intrinsic and extrinsic signaling—that lead to single-cell heterogeneity along the spectrum of these states (9, 10, 13–16). Together, these observations provide supportive evidence for a

[1]Mass General Cancer Center, Harvard Medical School, Charlestown, Massachusetts. [2]Division of Gastroenterology, Massachusetts General Hospital, Harvard Medical School, Boston, Massachusetts. [3]Department of Medicine, Massachusetts General Hospital, Harvard Medical School, Boston, Massachusetts. [4]Department of Radiology, Massachusetts General Hospital, Harvard Medical School, Boston, Massachusetts. [5]Department of Radiation Oncology, Massachusetts General Hospital, Harvard Medical School, Boston, Massachusetts. [6]Department of Pathology, Massachusetts General Hospital, Harvard Medical School, Boston, Massachusetts. [7]Biostatistics, Massachusetts General Hospital, Harvard Medical School, Boston, Massachusetts. [8]Center for Systems Biology, Massachusetts General Hospital, Harvard Medical School, Boston, Massachusetts.

Eric W. Lin, Priyadarshini Pathak, Aileen O'Shea, and Beatrice Awasthi contributed equally as co-first authors.

William L. Hwang, Mukesh G. Harisinghani, David T. Ting, and Colin D. Weekes contributed equally as co-senior authors.

Corresponding Authors: Colin D. Weekes, Mass General Cancer Center, 55 Fruit Street, Boston, MA 02114. E-mail: cdweekes@mgh.harvard.edu; David T. Ting, Mass General Cancer Center, 149 13th Street, Room 6003, Charlestown, MA 02129. E-mail: dting1@mgh.harvard.edu; Mukesh G. Harisinghani, Department of Radiology, Massachusetts General Hospital, 55 Fruit Street, Boston, MA 02114. E-mail: mharisinghani@mgh.harvard.edu; and William L. Hwang, Department of Radiation Oncology, Massachusetts General Hospital, 185 Cambridge Street, Boston, MA 02114. E-mail: whwang@mgh.harvard.edu

Clin Cancer Res 2026;32:869–82

doi: 10.1158/1078-0432.CCR-25-2052

Translational Relevance

This study provides initial evidence highlighting the potential of targeting pancreatic ductal adenocarcinoma (PDAC) plasticity as a treatment strategy. Specifically, glycogen synthase kinase 3β (GSK-3β) inhibition with elraglusib promotes PDAC cell transition from quasi-mesenchymal to epithelial transcriptional states to abrogate FOLFIRINOX resistance. Additionally, the tumor growth inhibitory effects of GSK-3β blockade coincide with the development of a tumor-suppressive immune microenvironment.

therapeutic strategy targeting chemotherapy-induced PDAC EMT as a cellular mechanism of acquired resistance.

Prior work by Brunton and colleagues (16) identified enrichment of glycogen synthase kinase 3β (GSK-3β) in QM PDAC models, and small-molecule inhibitors of GSK-3β have previously demonstrated sensitivity in QM PDAC cell lines. GSK-3β promotes PDAC EMT by suppression of E-cadherin–β-catenin complex formation via β-catenin phosphorylation, in addition to direct modulation of NF-κB–mediated transcription of EMT transcription factors snail family zinc finger 1 and 2 (*SNAI1* and *SNAI2*), zinc finger E-box binding homeobox 1 (*ZEB1*), and lymphoid enhancer-binding factor 1 (*LEF1*; refs. 17, 18). Meanwhile, prior preclinical work with the angiotensin II receptor blocker losartan (LOS) had shown improved tumor vascularization by modulating the stromal microenvironment, thereby enhancing chemotherapy delivery in PDAC mouse models (19). This led to a phase II trial of FOLFIRINOX plus LOS in locally advanced PDAC, with a striking median PFS of 17.5 months and median overall survival (OS) of 30.0 months (20). We hypothesized, therefore, that the addition of a GSK-3β inhibitor to FOLFIRINOX plus LOS would greatly enhance response rates and outcomes in patients with PDAC.

Elraglusib [(ELRA) 9-ING-41, Actuate Therapeutics, Inc.] is a GSK-3β small-molecule inhibitor with antitumor activity (21). Preclinical evaluation demonstrates that combination treatment with gemcitabine led to significant growth inhibition *in vitro* and *in vivo* through impaired ATR activation and degradation of the ATR-interacting protein TopBP1 (22). In a recently reported randomized phase II study, the addition of ELRA to gemcitabine and nab-paclitaxel as first-line therapy improved the OS of patients with metastatic PDAC in comparison with gemcitabine and nab-paclitaxel (HR = 0.63, log-rank $P = 0.01$; ref. 23). Here, we show, using a preclinical model, that ELRA shifts PDAC cells from a QM to E state and synergizes with FOLFIRINOX therapy. Furthermore, we present early data from a clinical trial highlighting the potential efficacy of combining ELRA with FOLFIRINOX plus LOS for the treatment of metastatic PDAC. Applying spatial transcriptomics and molecular phenotyping techniques, we found changes toward the E state in clinical trial samples concordant with preclinical cell line models. Finally, we combined the aforementioned molecular analysis with single-nucleus RNA sequencing (snRNA-seq) and ferumoxytol-enhanced MRI (F-MRI) to clinically evaluate changes in the tumor immune microenvironment in these patients. This proof-of-concept study provides initial evidence that GSK-3β blockade has a multimodal effect of modulating PDAC plasticity while promoting the development of a tumor-suppressive immune microenvironment to enhance the effects of cytotoxic chemotherapy.

Patients and Methods

Patient selection

All patients were enrolled after providing written informed consent to study team members. The study was conducted in accordance with the International Council for Harmonisation of Technical Requirements for Pharmaceuticals for Human Use Good Clinical Practice guidelines to ensure the ethical treatment of all patients participating in clinical research. We enrolled patients at least 18 years old with histologically or cytologically confirmed untreated metastatic PDAC, Eastern Cooperative Oncology Group performance status ≤1, and adequate organ function who had no prior therapy for PDAC in any form. Participants were required to have measurable disease as defined by RECIST 1.1. Prior treatment with angiotensin receptor blockers (ARB) for hypertension was allowed. Patients assigned to a non-LOS–containing treatment arm were changed to an antihypertensive medication that is not in the class of ARBs. Patients with known or suspected deleterious germline or somatic BRCA-mutated PDAC, with known tropomyosin receptor kinase fusion–positive PDAC, or with known deficient mismatch/microsatellite instability or high tumor mutation burden PDAC were excluded. Please refer to the protocol for a full list of inclusion/exclusion criteria.

Study design and treatment

The presented data were from six patients treated in a safety cohort of an open-label, multiarm, randomized phase II clinical trial, NCT05077800, conducted at the Massachusetts General Hospital Cancer Center in Boston, MA. A total of seven patients were enrolled between March 9, 2022, and June 10, 2022. One patient experienced disease progression and transitioned to comfort care prior to starting study treatment. Six patients treated in the independent safety cohort were directly assigned to treatment with the combination of modified FFX, ELRA, and LOS in a 14-day cycle. Modified FOLFIRINOX consists of day 1 intravenous administration of oxaliplatin 85 mg/m^2, leucovorin 400 mg/m^2, irinotecan 150 mg/m^2 and 5-FU continuous intravenous infusion (CIVI) 2,400 mg/m^2 over 46 hours every 14 days per standard of care. ELRA 9.3 mg/kg was administered on days 1 and 8 of each 14-day cycle. ELRA was administered intravenously prior to CIVI 5-FU pump connection. LOS was administered orally daily at a dose of 50 mg. LOS was dosed at 25 mg orally daily for days 1 to 7 of cycle 1. LOS was titrated to 50 mg daily on day 8 if blood pressure criteria were met. Pegylated or nonpegylated granulocyte stimulating factor (e.g., Neulasta, Neupogen, Udenyca, Granix) was administered per institutional standards. Patients transitioned to maintenance CIVI 5-FU therapy plus a biologic agent within 2 weeks after completion of 12 cycles of FOLFIRINOX (complete therapy 1) without evidence of disease progression. Patients restarted FOLFIRINOX (complete therapy 2) at the time of disease progression on maintenance therapy (MT) within 2 weeks of completion of the last cycle of MT. Treatment withdrawal for disease progression was based on disease progression occurring while the patient received complete therapy unless the patient could no longer receive complete therapy due to toxicity. Patients underwent biopsy of the metastatic tumor site at baseline, prior to cycle 5 day 1 (cycle 4 days 9–14), prior to starting MT (cycle 12 days 9–14), and at the time of disease progression, resulting in the patient going off study treatment. Patients also underwent F-MRI at the same time points as the metastatic tumor biopsy. Blood was obtained for biomarker analysis on day 1 of cycles 1, 2, 3, and 4 and day 1 of odd-numbered cycles beyond cycle 4. In

addition, blood was obtained at the transition to MT, disease progression (start of complete therapy 2), and off treatment. Following the evaluation in the safety cohort, 50 patients were enrolled for a multiarm noncomparator phase II study, with patients randomly assigned in a 1:3:3:3 manner to receive treatment with FFX alone ($n = 5$), FFX + LOS ($n = 15$), FFX + ELRA ($n = 15$), or FFX + LOS + ELRA ($n = 15$).

Assessments

Participants were seen weekly for clinical assessments and were evaluated for radiographic response every four cycles. Patients were followed every 6 months for survival until death, withdrawal of consent for follow-up, or up to 5 years. All adverse events (AE) were monitored from registration until 30 days after treatment and were graded according to the NCI Common Terminology Criteria for Adverse Events, version 5.0. Following disease progression, patients were followed per protocol for survival (details in the protocol).

Study endpoints

The primary endpoint of the safety cohort was to evaluate the treatment-related AEs and determine the recommended phase II dose of the combination therapy of FOLFIRINOX, ELRA, and LOS. The six patients were treated with the standard dose of FOLFIRINOX (Table 6.1), LOS, and ELRA. If more than one dose-limiting toxicity (DLT) occurred within the first two cycles of treatment, six patients were treated at dose level −1 of FOLFIRINOX, LOS 25 mg, and ELRA 7 mg/kg. If two or more DLTs were noted within the first two cycles of treatment, no further patients would be treated with the combination. Secondary endpoints include PFS, time on MT, objective response rate (ORR), and OS. PFS is defined as the time from study entry to the earliest occurrence of progressive disease while receiving complete therapy with FOLFIRINOX-based therapy or death due to any cause. Progressive disease must be documented objectively in one or more local and/or distant sites. Patients receiving maintenance 5-FU–based therapy who develop disease progression will return to FOLFIRINOX-based therapy and will not be censored for PFS outcome estimation. Time on MT is defined from the start of maintenance 5-FU–based therapy to the time of objective disease progression. ORR is defined as the proportion of patients who have a partial response (PR) or complete response per RECIST 1.1 criteria.

Statistical analysis

Six patients in the safety cohort were evaluated independently to assess the safety of the combination therapy of FOLFIRINOX, ELRA, and LOS. Secondary endpoints to be evaluated in the multiarm portion of the study will include PFS, ORR, time on MT, and OS. If a patient is lost to follow-up or withdraws from the study or the study is ended prior to progression/death, the patient will be considered censored at their last recorded follow-up. The distribution of PFS and OS will be calculated with 95% confidence intervals using Greenwood's formula and depicted using Kaplan–Meier survival curves. Survival curves will be compared with historical data using a one-sample log-rank test. Because the study sample size is not powered for comparing the OS, comparisons with historical data will be performed for exploratory purposes. Radiographic ORR per RECIST 1.1 will be reported along with the corresponding binomial exact 95% confidence intervals. Statistical analyses were performed using SAS version 9.4 (SAS Institute, RRID: SCR_008567).

Cell lines

Patient-derived PDAC cell lines (PDAC3, PDAC6, and PDAC9) were derived from metastatic ascites from patients under a discarded tissue protocol in accordance with the Massachusetts General Hospital Institutional Review Board (IRB) protocol 2011P001236, as previously described (24). Cells were cultured in DMEM (Gibco, cat. #11995065) supplemented with penicillin (100 U/mL) and streptomycin (100 μg/mL; 1×; Gibco, cat. #15140122) and 10% fetal bovine serum (FBS). Cell cultures were regularly tested for mycoplasma contamination with the MycoAlert PLUS Mycoplasma Detection Kit (Lonza, cat. #LT07-705).

In vitro drug treatment studies

PDAC3, PDAC6, and PDAC9 cells were plated at a density of 1×10^3 cells/well (100 μL media) in 96-well clear round-bottom ultralow attachment (ULA) microplates (Corning, cat. #7007). After 24 hours of incubation, cells were treated with different concentrations and combinations of drugs and/or vehicle at a total volume of 20 μL drug/well. After 7 days of drug treatment, luminescence cell viability assays were performed using CellTiter-Glo 3D (Promega, cat. #G9683), in accordance with the vendor's recommendations. After 5 minutes of incubation on a shaker at ambient temperature, microplates were read using a SpectraMax Multi-Mode Microplate Reader (Molecular Devices) and SoftMax software. Luminescence reading matrices were exported as Excel (RRID: SCR_016137) files to calculate the percent inhibition values and then further exported either to GraphPad Prism 10.2.3 (RRID: SCR_002798) or the SynergyFinder Plus web application (https://synergyfinder.org; ref. 25) for final data analysis. The drugs used were ELRA (MedChem Express, cat. #HY-113914) and FOLFIRINOX (FFX), a chemotherapy combination including 5-FU (Invitrogen, cat. #sud-5fu), Irinotecan (Cayman Chemical Company, cat. #14180), and Oxaliplatin (Sigma-Aldrich, cat. #09512). A 1× dose of FFX is composed of: 5-FU 43.4 μmol/L, Irinotecan 0.4 μmol/L, and Oxaliplatin 0.323 μmol/L. Two types of dose-response studies were performed. In both studies, the drugs were administered in 8 doses of ½ serial dilutions. For ELRA, the range of 8 doses of ½ serial dilutions was from 0.625 to 1.0 μmol/L/vehicle (DMSO, Sigma-Aldrich, cat. #D8418). For FFX the range of 8 ½ serial dilutions were from 1× to 0×/vehicle (regular media). In the first type of dose-response study, cell lines were treated with three conditions: FFX alone, ELRA alone, and a combination of FFX and ELRA. The study was performed in three biological replicates, each with three or four technical replicates per cell line (PDAC3, PDAC6, PDAC9). The Excel results (% Inhibition) were imported into GraphPad Prism 10.2.3 for nonlinear regression analysis (curve fit), with the X values representing $\log_2$ concentrations of the FFX ½ dilution series and the Y values representing cell viability responses. In the second type of dose-response study, a 64 combination microplate layout was used, with each well representing a unique drug combination resulting from the 8 × 8 ½ serial dilution matrix (with constant FFX doses in columns and constant ELRA doses in rows). The study was performed in two or three biological replicates per cell line. The Excel results (% Inhibition) were uploaded to the SynergyFinder Plus web application (https://synergyfinder.org; ref. 24) to generate dose–response matrices and synergy distributions using the Loewe additivity model. Wells with a synergy score ≥10 were considered to represent a synergistic effect for the corresponding dose combinations.

Bulk RNA-seq

PDAC3, PDAC6, and PDAC9 cells (2×10^5 per well) were prepared—in triplicate—in six-well ULA culture dishes in 3D media to allow tumorsphere formation. Similar to above, after 24 hours of

incubation, cells were treated with ELRA (at 0.625 and 1.25 μmol/L) or vehicle (DMSO). After 10 days of treatment, tumorspheres were collected, and RNA was extracted using the miRNEasy Mini Kit (QIAGEN), including the optional on-column DNase treatment (QIAGEN). RNA quality was analyzed using the Bioanalyzer 2100 (Agilent Technologies). To generate libraries for total RNA-seq, the Illumina Smarter Stranded Total RNA-seq kit version 2 (cat. #634413) was used according to the manufacturer's instructions. Pooled libraries were sequenced on an Illumina NextSeq 500 sequencer.

Raw Illumina reads were quality-filtered and aligned as per prior studies in the lab (2). The downstream analysis was carried out in R (RRID: SCR_001905), using DESeq2 for differential expression analysis (3). The R package clusterProfiler (RRID: SCR_016884) was used for gene set enrichment (pathway) analysis (4). Heatmaps were plotted using the R package ComplexHeatmap (RRID: SCR_017270; ref. 5).

RNA *in situ* hybridization

Formalin-fixed, paraffin-embedded (FFPE) tissue sections from four patients were stained using RNA in situ hybridization (RNA ISH; ACD RNAscope 2.5 LS Duplex Reagent Kit - RED/BROWN, RRID: AB_2136278) on a Leica BOND RX automated stainer, with epitope retrieval performed under EDTA-based pH 9 conditions. A PDAC xenograft control was included with each batch of patient slides as a staining control. Probes for the EMT ISH Pancreatic Cancer Pool (Epi-C1 QM-C2, cat. #321762) were used. The E probe pool (CDH1, EPCAM, KRT5, KRT7, KRT8, KRT19) was visualized using the DAB chromogen (Leica BOND Polymer Refine Detection, DS9800), whereas the mesenchymal probe pool (FN1, SERPINE1, CDH2) was labeled with the Fast Red chromogen (BOND Polymer Refine Red Detection, DS9390). Whole images of stained slides were acquired at 40× (0.26 μm/pixel) resolution using a MoticEasyScan Infinity digital pathology scanner.

RNA-ISH quantification

The EMT dual ISH stained images were analyzed using the HALO digital image quantification software platform (RRID: SCR_018350). Annotated tumor regions were verified by a pathologist (B.K. Patel). Large folds, debris, fat, muscle, and normal tissue were excluded from quantification. The HALO AI DenseNet convolutional neural network classifier was trained to distinguish tumor glands from stroma within the annotated tumor regions and was manually validated afterward. The HALO ISH module version 4.2.11 was used to quantify ISH markers. Nuclear detection was performed using either the default artificial intelligence (AI) nuclear segmentation classifier or a custom AI nuclear segmentation classifier (HALO AI version 4.0.5107.318) for cases in which hematoxylin nuclear staining was weak. RNA-ISH positivity was based on signal intensity and dot size within a cell, with brighter and larger dots having more weight and staining patterns of the color-deconvolved image component of each chromogen (DAB, E probe pool; FastRed, mesenchymal probe pool). Cells that were double-positive for E and mesenchymal stains were considered QM.

Following analysis, object tables were exported into GraphPad Prism 10.2.3. The QM percentage per patient case was calculated as the ratio of double-positive cells (brown and red) to the total glandular E/single-positive cells (brown) and represented as part of a whole via a pie chart. For each patient case, representative tumor regions, with and without the classifier mask, were captured using the Figure Maker tool option and exported as .jpg files.

Specimen acquisition and histologic review

This discarded excess tissue study was approved by the IRB at the Dana-Farber Harvard Cancer Center (IRB 21-350). Serial sections from FFPE blocks were then made, with the first section stained using hematoxylin and eosin (H&E) and evaluated by a pathologist (B.K. Patel).

Spatial transcriptomics data generation

We used the GeoMx Digital Spatial Profiler platform (NanoString Technologies; RRID: SCR_021660) to collect genetic information from transcribed mRNA. This involved staining the slide with the GeoMx Human Whole Transcriptome Atlas (a mix of unique oligo-labeled probes against 18,676 mRNAs). This was followed by staining with fluorescent morphology markers, PanCK (NanoString), CD45 (NanoString), and alpha-smooth muscle actin (clone 1A4; Novus Biologicals, cat. #IC1420R, RRID: AB_3654722, conjugated with lyophilized Alexa Fluor 647 mix ab274049, Abcam) to visualize the E, immune, and fibroblast compartments, respectively, at different emission spectra. After staining, multiple regions of interest (ROI) were marked out with H&E as a reference. A total of 72 ROIs were marked out, following which the instrument accurately segmented the ROIs into distinct immune/E/fibroblast "areas" of interest (AOI). This was followed by the collection of the barcodes (attached to oligos by ultraviolet light-cleavable bonds) onto a 96-well collection plate. The sampled oligos were then pooled following the NanoString GeoMx-NGS Readout Library Prep User Manual (MAN-10117-03). Illumina's i5 × i7 dual indexing system was used for amplification and ligation of the adapters. Quantitation of the final library was done by qPCR using KAPA estimation (KAPA code: KK4854, Roche, cat. #07960298001) with the Roche LightCycler 480 program and was eventually sequenced with a 1% PhiX spike-in on a NextSeq 500/550 using a 2 × 75-cycle Mid-Output version 2.5 flow cell, following instructions in the Illumina NextSeq manual (15048776, version 16). The generated FASTQ files were processed to generate target probe-specific count files and saved in Data Coordination Center (DCC) format.

Nanostring computational methods

Probes were collapsed to the geometric mean of each target after removing outliers using a Grubbs test per gene across AOIs. AOIs with low read alignment quality, low total read counts, and low segment area were excluded from the analysis. The data were quantile normalized such that each AOI has the same 75th percentile of expression. AOIs were grouped by segment (epithelial, immune, fibroblast) and clustered using the unweighted pair group method with arithmetic mean (UPGMA) on the top 900 most variable genes. Clear distinctions were observed for the immune and E segments, and groups were defined based on the first and second dendrogram separations, respectively.

The epithelial compartment

Differential expression analysis was then performed on every combination of the three epithelial groups using a Mann–Whitney test, and significant genes were defined as having an FDR-adjusted *P* value of less than 0.05 and at least a twofold change in mean expression. Gene set enrichment analysis (GSEA) was performed using the clusterProfiler R package (RRID: SCR_016884). Gene set meta scores were then generated for the Moffitt EMT gene set by calculating the difference in mean *z*-score of the genes from the two Moffitt subtypes for each AOI.

The fibroblast compartment

Differential expression analysis was performed as above. In addition, an inflammatory cancer-associated fibroblast (iCAF)/myofibroblastic CAF (myCAF) gene subset was utilized to specifically assess CAF subtypes in available AOIs.

The immune compartment

Immune cell subtype composition was estimated using the SpatialDecon R package version 1.6.0 (RRID: SCR_026836).

snRNA-seq library preparation

snRNA-seq was performed by the Mass General Brigham (MGB) Biobank Genomics Core. Sample preparation for snRNA-seq was performed using the Evercode Low Input Cell and Nuclei Fixation version 3 (Parse Biosciences, #ECLN3301) and Evercode Whole Transcriptome version 3 (Parse Biosciences, #ECWT3300) kits. First, tumor biopsies were lysed and nuclei isolated on a per-sample basis. For tumor biopsy lysis and nuclei isolation, Salts + Tricine (STc) and NP40 + Salts + Tricine + Polyamines (NSTcPA) buffers were prepared as previously described (25). Frozen tissues were then transferred into 500 μL of NSTcPA buffer containing DNA and RNA inhibitors (New England Biolabs, #M0303L, and Millipore Sigma, #3335402001) and minced for 8 minutes. Minced tissues were pipetted over a 40 μmol/L filter (Corning, #431750) into a 50 mL conical tube. The well was washed twice with 1 mL of NSTcPA buffer and twice with 1 mL of Salts + Tris (ST) buffer and pipetted over the same filter for each subsequent wash. Subsequently, 1 mL of ST buffer was pipetted over the filter twice to further dilute the sample. The sample was then transferred to a 15 mL conical tube and centrifuged at 500 × *g* for 5 minutes at 4°C, with deceleration set to 5. The supernatant was removed, and the pellet was resuspended in 100 to 200 μL of PBS (Corning, #21-040-CV) /1% BSA (Sigma-Aldrich, #A9418) and then pipetted through a 35 mmol/L FACS tube.

Nuclei were quantified using a disposable C-Chip hemocytometer (VWR, # DHCN015), and up to 100,000 nuclei per sample were immediately fixed using the Evercode Low Input Cell Fixation kit according to the manufacturer's instructions. Nuclei samples were then stored at −80°C until all samples were ready to proceed with library preparation. Sequencing library preparation with 12,500 cells per library was performed with the Evercode Whole Transcriptome version 3 kit according to the manufacturer's instructions. Sublibrary quality control and quantification were performed using a Qubit fluorometer (Qubit 4: Thermo Fisher Scientific, #Q33226, and Qubit Flex: #Q33327), Agilent 4200 TapeStation (Agilent, #G2991BA), and KAPA qPCR analysis (Roche, #07960140001), and sublibraries were then pooled to 4 nmol/L for sequencing based on qPCR results. Seven sublibraries were pooled and submitted for sequencing in total.

snRNA-seq

snRNA-seq was performed by the MGB Biobank Genomics Core. Pooled snRNA sequencing sublibraries were sequenced using a NovaSeq 6000 S2 flow cell with 200 cycles (65 + 8 + 8 + 58). Samples were loaded onto the sequencer at 450 nmol/L with a 5% PhiX spike-in.

snRNA-seq data processing

FASTQ files were prepared using bcl2fastq2 conversion software version 2.20 via Illumina BaseSpace sequencing hub. Preprocessing and alignment of FASTQ files were performed using the Parse Trailmaker Pipeline module version 1.4.1. Briefly, FASTQ files were provided to the pipeline, and transcript sequences were aligned to the GRCh38 reference genome. Count matrices filtered according to sample-specific barcode thresholds established within the pipeline were then downloaded for downstream analyses in R.

snRNA-seq cell type annotation

snRNA-seq analysis was performed using Seurat. For quality control filtering, count matrices were filtered to include only genes with minimum expression in greater than or equal to 100 cells and $\log_{10}$GenesPerUMI greater than or equal to 0.8. Additional quality control filtering was performed to include cells with $n_{transcripts}$ and $n_{genes} > 300$, $n_{transcripts} < 15{,}000$, $n_{genes} < 5{,}000$, and mitochondrial genes <10%. Doublet identification was performed using scDblFinder (12), and doublets were removed prior to further analysis. Subsequently, the counts matrix was normalized using NormalizeData (normalization.method = "LogNormalize" and scale.factor = 10,000), the top 2,000 variable features were identified using FindVariableFeatures (selection.method = "vst"), and the counts matrix was scaled using ScaleData.

For cell type annotation, iterative subclustering was performed across multiple rounds, and cell type labels were assigned to clusters based on marker gene signatures (25–29).

During the first round of annotation, E and non-E cell clusters were identified. First, dimensionality reduction was performed using principal component analysis (PCA), followed by Uniform Manifold Approximation and Projection for Dimension Reduction (UMAP) to visualize individual nuclei. For clustering, a K-nearest neighbor graph was first constructed to delineate cellular neighborhoods based on similar features using the FindNeighbors function, followed by the identification of distinct cellular clusters using the FindClusters function with Louvain clustering.

The malignancy of epithelial cells was confirmed using infercnvpy (https://github.com/icbi-lab/infercnvpy). To that end, the raw counts matrix and gene and cell type annotations were used to create an AnnData object in Python, and the data were normalized and logarithmized using the sc.pp.normalize_total and ss.pp.log1p functions from Scanpy (30). The cnv.tl.infercnv function was run with all non-E cells used as reference cells. Based on the infercnvpy analysis, all E cells were treated as malignant cells.

Non-epithelial cells were isolated and further subtyped into fibroblast, immune, endothelial, and hepatocyte classes over multiple rounds of subclustering. Immune cells were further subtyped into lymphoid and myeloid groups, which were then each subclustered into specific lymphoid and myeloid cells. For each round of subclustering, the top variable features were reidentified, the data were rescaled, and dimensionality reduction by PCA was again performed. Following PCA, batch correction was performed for all rounds of nonmalignant subtyping using Harmony (31) with parameters theta = 10, lambda = 0.5, and 12 iterations of clustering. Nuclei were visualized by UMAP, and clusters were identified by FindNeighbors and FindClusters as described above. For UMAP and Leiden clustering, the resolution and number of dimensions were empirically determined. Unclassified or noisy cells were removed from further analysis across multiple rounds.

Cell type annotation was performed for patients 2, 3, 4, 6, and 7, in addition to an additional baseline sample. Due to unacceptably low cell counts for patient 3 cycle 4 day 1 and the additional baseline samples, patient 3 and the additional sample were not included in downstream analyses.

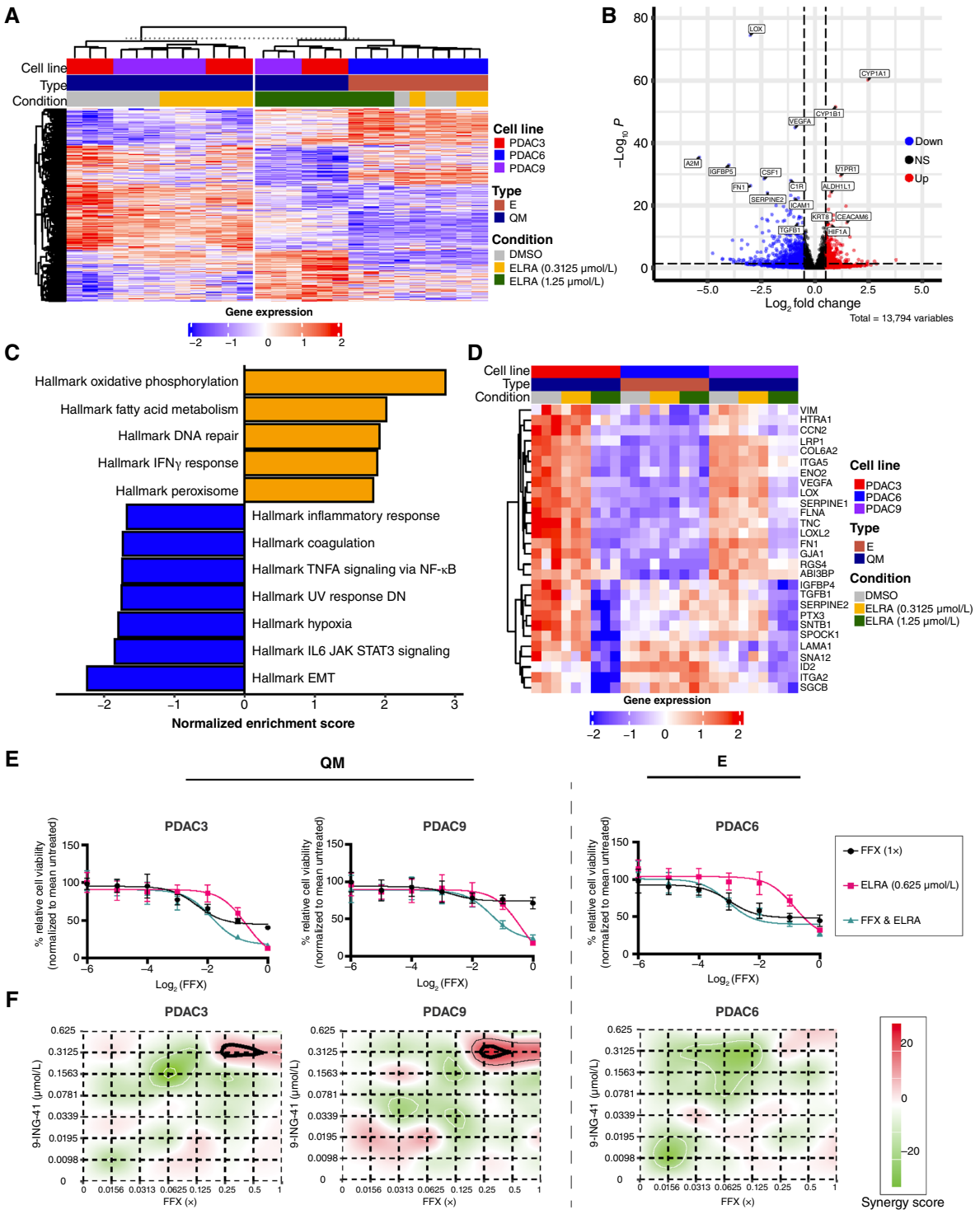

Figure 1.

GSK-3β inhibition with ELRA modulates EMT plasticity in PDAC cell lines. **A,** Heatmap depicting DEGs (1,605 total DEGs with adjusted *P* value < 0.1, *z*-score shown by color) by cell line and treatment, with unsupervised hierarchical clustering. E and QM baseline cell types are designated. **B,** Volcano plot showing significant DEGs in QM cell lines treated with ELRA (red) vs. DMSO (blue), with selected genes of interest labeled. NS, nonsignificant. **C,** Bar plot of significantly altered Hallmark (MSigDB) pathways via GSEA of DEGs in QM cell lines in ELRA (orange) vs. DMSO (blue). **D,** Significantly altered Hallmark EMT genes with hierarchical clustering ordered by cell line and treatment condition. **E,** PDAC cell viability with increasing doses of FFX alone, ELRA alone, or both. Full (1×) FFX dose = 5-FU 34.4 μmol/L, irinotecan 0.4 μmol/L, oxaliplatin 0.323 μmol/L. Full (1×) 9-ING-41 dose = 0.625 μmol/L. **F,** Synergy plot demonstrating dose-based synergy score (Loewe model) between FFX and ELRA, in which scores >10 represent synergy, by PDAC cell line.

MRI imaging protocol

Ferumoxytol (Feraheme, AMAG Pharmaceuticals) is an ultrasmall iron oxide nanoparticle with unique pharmacokinetics, metabolism, and imaging properties. Previous studies have demonstrated that ferumoxytol induces signal changes on MRI, which correspond to macrophage accumulation of the nanoparticle, 24 hours after injection (32).

F-MRI was obtained at baseline (prior to cycle 1 day 1), after four cycles of therapy [prior to cycle 5 day 1 (C5D1)], and at the time of documented disease progression.

Ferumoxytol administration

Ferumoxytol was administered intravenously as a slow infusion at a dose of 6 mg/kg. The solution, available in a 30 mg/mL concentration, is provided in single-use vials, each containing 510 mg of elemental iron in 17 mL. It is stored at controlled room temperatures between 20°C and 25°C (68°F and 77°F), with acceptable excursions ranging from 15°C to 30°C (59°F to 86°F). For this study, ferumoxytol was diluted with 20 cc of saline and administered over a 15-minute period via slow injection.

Image acquisition

Imaging was conducted at two consecutive time points. The first time point (day 0) involved an upper abdominal MRI using a standard protocol with anatomic sequences. Additionally, high-resolution, narrow field-of-view diffusion-weighted imaging sequences (ZOOMit, Siemens Healthineers) were acquired both before and after ferumoxytol administration. T2* maps were generated after injection. To complement this, a free-breathing, high-resolution, post-contrast T1-weighted sequence (GRASP VIBE, Siemens Healthineers) was captured during dynamic ferumoxytol infusion. The second time point (24–48 hours after ferumoxytol injection) involved a repeat of both the narrow field-of-view images and ZOOMit sequences.

Image analysis

Imaging was analyzed using a standard clinical PACS (Visage Imaging Client, version 7.1, Visage Imaging) with all clinically available image manipulation tools (window and level, cross-correlation, zoom, and scrolling, for example). T2* maps were generated, and values were measured using a standard two-dimensional 1 cm ROI placed over the pancreatic lesion and in the normal pancreas. Absolute T2* values were obtained from the lesion at time point 1 (the day of ferumoxytol injection) and time point 2 (24–48 hours after injection). In addition, the difference in T2 * values between time point 1 and time point 2 was obtained. These values were also obtained for hepatic metastases. A representative lesion that corresponded to the lesion percutaneously sampled prior to cycle 1 day 1 initiation of therapy was chosen.

Table 1. Demographic and baseline characteristics of patients.

	Treated patients (*N* = 6)
Age, years	
Median (range)	63.5 (51–66)
Sex, *n* (%)	
Male	3 (50)
Female	3 (50)
Race/ethnicity, *n* (%)	
White/not Hispanic	5 (83.33)
Black/African American	1 (16.66)
Eastern Cooperative Oncology Group performance status, *n* (%)	
0	4 (66.66)
1	2 (33.33)
Pancreatic tumor location, *n* (%)	
Body/tail	5 (83.33)
Head/neck	1 (16.66)
Biliary drain or stent, *n* (%)	
Yes	1 (16.66)
No	5 (83.33)
Metastatic sites, *n* (%)	
Liver	6 (100)
Lymph nodes	3 (50)
Peritoneum	1 (16.66)
Lung	1 (16.66)
Level of carbohydrate antigen 19-9, *n* (%)	
Normal	2 (33.33)
Elevated, <59 × ULN	0 (0)
Elevated, >59 × ULN	4 (66.66)

Abbreviations: *n*, number of patients; *N*, total number of patients; ULN, upper limit of normal.

Results

GSK-3β inhibition with ELRA can shift the EMT state in PDAC cell lines

To understand the effect of ELRA on PDAC cells, we utilized 3D tumorspheres of PDAC cell lines comprising both E and QM states (E: PDAC6; QM: PDAC3, PDAC9) for which we have previously described EMT heterogeneity and response to therapy (10). We treated cells with IC_{50} (0.3125 μmol/L) and IC_{100} (1.25 μmol/L) doses of ELRA (Supplementary Fig. S1A). We next analyzed gene expression patterns in response to treatment using bulk RNA-seq. We found that gene expression varied significantly between cell lines (Supplementary Fig. S1B), with ELRA-induced changes more apparent at the higher IC_{100} dose. With ELRA treatment, there were 719 differentially expressed genes (DEG), which revealed a shift in the transcriptomic profile in QM cell lines PDAC3 and PDAC9 toward the E cell line PDAC6 (**Fig. 1A**). Among these DEGs were multiple downregulated genes involved in EMT promotion in cancer, including *LOX*, *IGFBP5*, *FN1*, *SERPINE2*, *ICAM1*, and *TGFB1* (**Fig. 1B**). Furthermore, genes associated with the E state, including *KRT8* and *CEACAM6*, were upregulated with GSK-3β inhibition. Other notable treatment-induced genes included *ALDH1L1* and *HIF1A*, which are involved in cell metabolism. In summary, we observed that ELRA is able to shift PDAC cells to an E cell state away from stem-like mesenchymal features enriched in 3D tumorsphere culture.

We then performed GSEA, revealing a strong downregulation of EMT along with IL6 and TNFα signaling (**Fig. 1C**). In contrast, ELRA led to the upregulation of oxidative phosphorylation and the IFNγ response. When visualizing gene expression among genes from the Hallmark EMT gene set, there was a clear dose-dependent shift in the QM cell lines PDAC3 and PDAC9 (**Fig. 1D**).

ELRA treatment synergizes with cytotoxic therapy in QM cells

Given that EMT has been previously shown to underlie chemoresistance to cytotoxic therapy, we hypothesized that combination therapy with ELRA could sensitize PDAC cells to FOLFIRINOX. To test this, we exposed PDAC cell lines to increasing doses of ELRA, FOLFIRINOX, and ELRA plus FOLFIRINOX. We found that although FOLFIRINOX monotherapy resulted in significant (>45%) resistance even at full dose in QM cell lines, the addition of ELRA

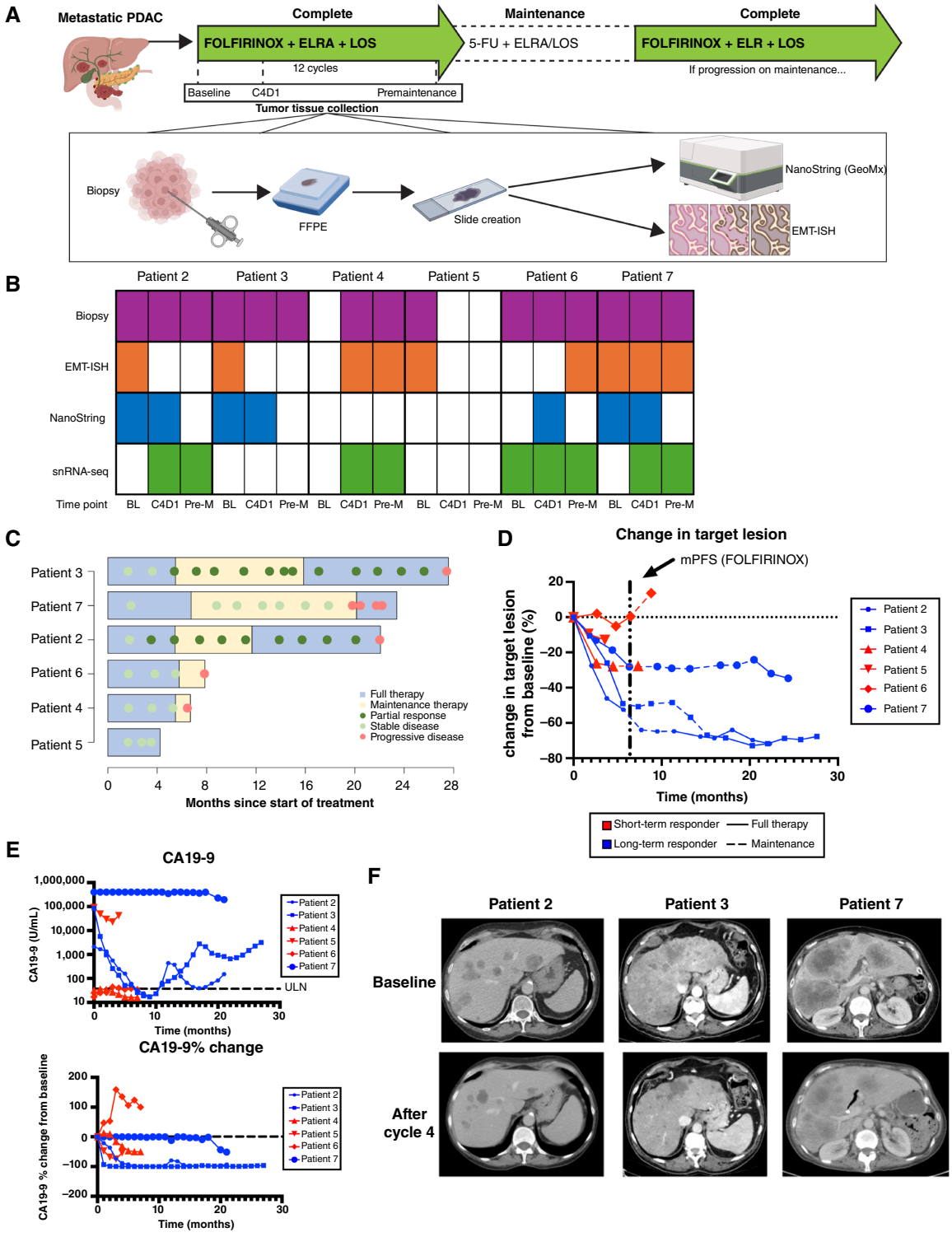

Figure 2.

ELRA in combination with FOLFIRINOX and LOS demonstrates clinical activity in patients with metastatic pancreatic adenocarcinoma. **A,** Clinical study design and timed serial tissue collection for downstream analysis using Nanostring (GeoMx) and EMT-ISH. **B,** Tissue sample collection and downstream processing timeline. **C,** Swimmer's plot of treatment duration and response in sampled patients with PDAC. **D,** Percentage change in the size of the target lesion by CT scan measured over time compared with baseline. Short-term (red) and long-term (blue) responders with historical median PFS of FOLFIRINOX shown (dotted black line). **E,** CA19-9 values (U/mL) and percentage change from baseline trend by patient over time (months). **F,** Representative CT staging scans at baseline and after cycle 4 in the three long-term responder patients. (Created in BioRender.com. Lin, E. [2025] https://BioRender.com/bodeo7r.)

Table 2. Overview of TEAEs in the safety population.

	Grade 1/2	Grade 3/4
	n/N (%)	*n/N* (%)
Hematologic		
Neutropenia	1/6 (16.66%)	1/6 (16.66%)
Thrombocytopenia	6/6 (100%)	0/6 (0%)
Anemia	2/6 (33.32%)	3/6 (50%)[a]
Nonhematologic		
Fatigue	3/6 (50%)	2/6 (33.32%)
Nausea	3/6 (50%)	1/6 (16.66%)
Vomiting	3/6 (50%)	0/6 (0%)
Diarrhea	5/6 (83.33%)	0/6 (0%)
Neuropathy		
Paresthesia (cold sensitivity)	6/6 (100%)	0/6 (0%)
Peripheral sensory neuropathy (neuropathy)	4/6 (66.66%)	0/6 (0%)
Transaminitis	6/6 (100%)	0/6 (0%)
Thromboembolism	1/6 (16.66%)	1/6 (16.66%)
Vision changes	5/6 (83.33%)	0/6 (0%)
Hypotension	1/6 (16.66%)	2/6 (33.32%)[a]

Abbreviations: *n*, number of patients; *N*, total number of patients; TEAE, Treatment-emergent AE.
[a]One patient with duodenal hemorrhage.

(at IC_{50} dose) led to a synergistic effect at half dose FFX (**Fig. 1E** and **F**). In the E cell line PDAC6, however, most of the killing effect was driven by FFX alone, with no additional benefit from ELRA.

Clinical activity of ELRA in patients with metastatic pancreatic cancer

The observation that ELRA synergizes with FOLFIRINOX by modulating EMT plasticity and shifting QM cells to a more E state provided a rationale for the combination of ELRA with FOLFIRINOX in patients. As part of a larger open label, four-arm, non-comparator phase II clinical trial studying the effects of combination therapy including FOLFIRINOX, ELRA, and LOS, we treated six of seven enrolled patients with treatment-naïve metastatic PDAC in a safety run-in cohort to assess treatment-related toxicities. Safety cohort characteristics are listed in **Table 1**. Clinical response, serum-based tumor marker assessments, and biopsy samples were obtained for further study (see "Patients and Methods"; **Fig. 2A** and **B**).

The combination of ELRA, LOS, and FOLFIRINOX achieved stable disease or better in 5 of 6 safety cohort patients during the first 6 months of therapy (**Fig. 2C**). In addition, a long-term (>6 month) response was observed in 3 of 6 patients, all of whom achieved a PR by RECIST criteria (**Fig. 2C** and **D**). This response was also maintained during the maintenance phase of therapy (5-FU, ELRA, LOS). The duration of response was at least 20 months in each of the long-term responders. There was a robust decline in the tumor marker CA19-9 in the partial responders (**Fig. 2E**). There was a mild increase in CA19-9 during the MT phase in these patients, but this was subsequently reduced by the resumption of complete FFX-based therapy (**Fig. 2E**). Radiologic response was clearly demonstrated in patients 2, 3, and 7 with aggressive forms of metastatic PDAC (**Fig. 2F**). Genomic data, available in 5 of 6 patients, showed driver *KRAS* oncogenic mutations in each patient, along with other known genetic aberrations (Supplementary Table S1). Importantly, the combination of FOLFIRINOX with ELRA and LOS was well tolerated, with no serious grade 3 or 4 AEs. One patient developed grade 3 venous thromboembolism, which was attributed to underlying pancreatic cancer. The temporary induction of a blue–black visual hue that spontaneously resolves within 24 hours represents a unique toxicity associated with ELRA administration. There were no grade 3 or 4 visual adverse effects (**Table 2**). Overall, these results provide early evidence that the addition of ELRA and LOS to FOLFIRINOX is safe and has potential clinical efficacy in patients with metastatic PDAC.

Treatment with ELRA, LOS, and FOLFIRINOX alters EMT and TGFβ signaling in patients with metastatic PDAC

To further characterize treatment-induced changes, we performed Nanostring (GeoMx), spatial transcriptomic profiling, and snRNA-seq on biopsy specimens from safety cohort patients. Slides were stained and divided into epithelial, immune, and fibroblast "AOI" or compartments for sequencing analysis (see "Patients and Methods"). There were significant global gene expression changes before and after the completion of cycle 4 treatment and prior to starting MT in both epithelial (tumor) and immune compartments (Supplementary Fig. S2A–S2C; Supplementary Table S2). The stromal compartment did not reveal any significantly altered genes after treatment with ELRA, though each patient and condition were not evenly represented (Supplementary Fig. S3A). Utilizing a subset of markers for inflammatory CAFs and myCAFs, patient 3 demonstrated increased myCAF gene expression before treatment, but this was not seen in patient 2 (Supplementary Fig. S3B).

Within the epithelial compartment, there were 8,264 significantly altered genes with treatment (**Fig. 3A**). When compared with ELRA-induced changes in PDAC cell lines (**Fig. 1**), there were 97 overlapping DEGs that were also concordant in the direction of change. These genes not only demonstrated a clear treatment effect but also indicated cell populations (cluster 1 vs. cluster 2) that may have differential responses to treatment. GSEA of biopsied tumors demonstrated downregulation of the previously identified ELRA-altered EMT pathway in the PDAC cell lines, as well as decreased TGFβ signaling (**Fig. 3B**). Of note, some significant pathways, including the DNA repair and coagulation pathways, were reversed in posttreatment biopsies compared with our PDAC cell lines treated with single-agent ELRA.

Clinical responsiveness to GSK-3β inhibition correlates with QM tumor state

Given the concordant changes in EMT after ELRA treatment in both preclinical and clinical settings, we hypothesized that the degree of clinical response may be correlated with an underlying QM tumor state. To investigate this, we analyzed the transcriptomic profiles of patients after treatment with ELRA. Interestingly, we found natural gene clusters that seemed to vary based on response status (**Fig. 3C**). Cluster 1 was enriched for genes upregulated in responders, which were associated with upregulated pathways including complement, fatty acid metabolism, and decreased KRAS signaling (Supplementary Fig. S2D). In contrast, cluster 2 seemed to represent genes upregulated in a nonresponder, patient 6. Further analysis using gene set enrichment highlighted pathways that were upregulated in this patient, including EMT and TGFβ signaling (**Fig. 3D**).

To validate our spatial transcriptomics analysis, we performed EMT RNA-ISH on baseline biopsy specimens from patients. We found that the two deep long-term responders, patient 2 and patient 3, had higher degrees of QM marker expression (60.35% and

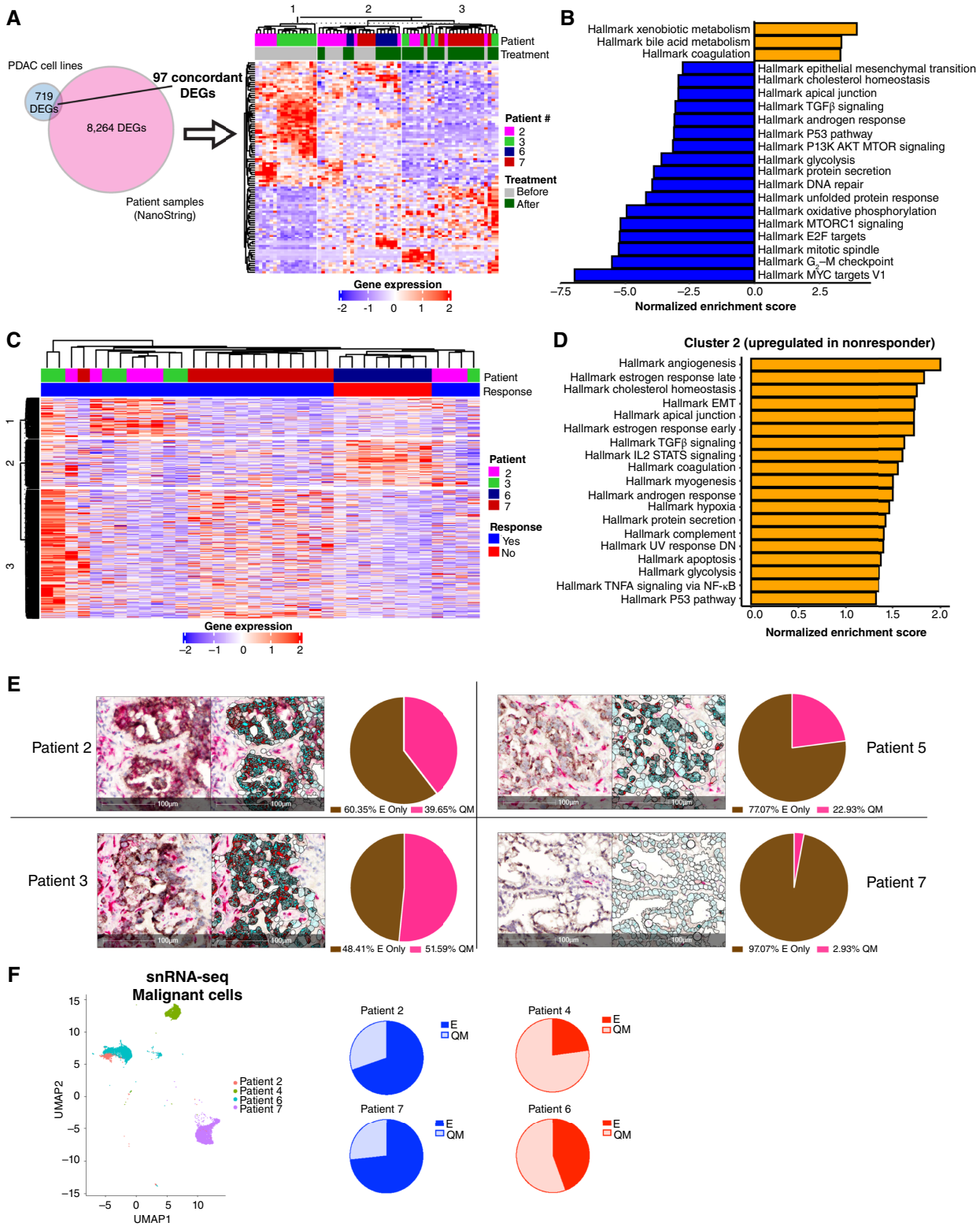

Figure 3.

Treatment response correlates with molecular features pertaining to the EMT state. **A,** Venn diagram demonstrating 97 concordant (same direction of change) overlapping DEGs (filtered by $|\log_2$ fold change$| > 0.5$, adjusted P value < 0.01) between PDAC cell lines and patients before and after treatment. Heatmap depicting gene expression (z-score) of these 97 DEGs by patient AOI and treatment condition, with unsupervised (*Continued on the following page.*)

48.41%, respectively) compared with the others studied (**Fig. 3E**). Moreover, patient 7, who had a ~30% response throughout the duration of follow-up, had a very small degree of QM marker expression at 2.93%. snRNA-seq analysis of biopsied tumors obtained prior to MT transition demonstrated the maintenance of the E transcriptional state in the long-term responder population (**Fig. 3F**; Supplementary Fig. S4A and S4B).

Overall, these data provide a clinical proof of concept that GSK-3β inhibition with ELRA in combination with standard cytotoxic therapy and potentially LOS may be an effective therapeutic strategy in metastatic PDAC of predominantly QM subtype.

Response to GSK-3β inhibition promotes a tumor-suppressive tumor immune microenvironment

Next, we aimed to quantitate dynamic changes in macrophage density in hepatic metastases using F-MRI as a clinical assay to monitor tumor-associated macrophage (TAM) trafficking associated with treatment. F-MRI was safely administered to the six patients treated in the safety cohort, with all patients receiving pre- and postinjection imaging, with the exception of patient 4 due to the development of back pain with injection. F-MRI quantification focused on liver metastases from which biopsies were obtained for spatial transcriptomics analysis. A representative imaging series from patient 2 is shown in **Fig. 4A** with an axial CT scan showing a liver metastasis (arrow), the same lesion seen on the T1 F-MRI image after contrast administration, and a subsequent ultrasound-guided liver biopsy for tissue analysis. A response to treatment was associated with an influx of macrophages, depicted by a decrease in T2* value at cycle 5 day 1 (**Fig. 4B** and **C**). Conversely, an efflux of macrophages was associated with treatment resistance and tumor growth (**Fig. 4D**). Long-term response to therapy was associated with at least a 40% decrease in T2* value at cycle 5 day 1 (**Fig. 4D**). Notably, the analysis of primary tumors and liver metastases across patients lacked concordance. Next, mixed cell deconvolution of the spatial transcriptomic profiling obtained from tumor biopsies after cycle 4 treatment demonstrated that the predominant cell type in the microenvironment of PDAC liver metastases was macrophages, but the proportion of macrophages was not consistently altered by treatment (**Fig. 4E**). snRNA-seq analysis of immune cells at cycle 12 prior to transition to MT (Supplementary Fig. S4C and S4D) demonstrated a trend toward a proportional increase in M1 TAMs in the long-term responder patients; however, due to the limited sample size, this observation will need to be confirmed in the phase II study (**Fig. 4F**). In addition, increased numbers of CD4 T cells, CD8 T cells, and NK cells were observed in the tumors of long-term responder patients (**Fig. 4G**). In summary, these data support the hypothesis that GSK-3β blockade–induced tumor growth inhibition coincides with the promotion of a tumor-suppressive immune microenvironment.

Discussion

The incorporation of combination chemotherapy regimens—FOLFIRINOX and gemcitabine plus nab-paclitaxel—as effective chemotherapy backbones for metastatic PDAC provided a promising foundation for the use of adjunct therapies to enhance response. Unfortunately, no new agents have demonstrated significant added benefit to these chemotherapy regimens since their introduction into the treatment paradigm over a decade ago. Still, the results of the COMPASS, PASS-01, and NeoPancONE trials provided a link between PDAC transcriptional subtyping and differential response to FOLFIRINOX in the metastatic and resectable disease settings (7, 8, 30, 33). In this article, we present preclinical and early clinical data supporting the targeting of EMT states with the GSK-3β inhibitor ELRA to shift PDAC from QM to E state and enhance FOLFIRINOX efficacy. The population of patients presented here are part of the initial safety cohort of clinical trial NCT05077800. We demonstrate that clinically achievable doses of ELRA induce an E transcriptional phenotype in QM PDAC cell lines (PDAC3 and PDAC9) but have little effect on an E PDAC cell line (PDAC6) in 3D tumorsphere cell culture. Furthermore, ELRA treatment of PDAC3 and PDAC9 was associated with the downregulation of *TGFB1* and other mesenchymal genes. In addition, there was downregulation of IL6 and TNFα signaling, both of which activate JAK/STAT3 and NF-κB pathways that lead to EMT, cancer progression (31, 34), and decreased sensitivity to FOLFIRINOX in cell culture.

Although based on a small number of patients, the results from the six patients treated in the NCT05077800 safety cohort receiving FOLFIRINOX, ELRA, and LOS provide early confirmatory patient data supporting our preclinical studies. Long-term responses associated with deep PRs for at least 20 months were observed in patients with predominantly QM tumors. Spatial transcriptomic analysis of tumor cell compartments from pre- and posttreatment biopsies revealed a reduction in EMT gene expression with an associated decrease in TGFβ, glycolysis, and proliferation signatures that are linked with more aggressive behavior. Interestingly, the third long-term responder (patient 7) had a tumor that comprised 97% E-type cells (**Fig. 3E**). This patient experienced a prolonged PR of ~30% reduction in tumor burden, which supports the possibility that FOLFIRINOX was the primary driver of therapeutic response in this patient, similar to our PDAC6 cell line culture data (**Fig. 1E** and **F**). In this case, ELRA may be functioning to suppress acquired FOLFIRINOX resistance by preventing the development of a substantive QM persister population over time. These observations support a model of chemically induced synthetic lethality, in which GSK-3β inhibition by ELRA drives QM PDAC tumor cells to an E transcriptional state, making E-predominant tumors more susceptible to FOLFIRINOX. The prolonged PFS observed in the long-term responders supports a hypothesis that targeting PDAC cell plasticity can suppress acquired resistance to FOLFIRINOX, which will be more comprehensively assessed upon the completion of this multiarm noncomparator phase II trial, NCT05077800.

GSK-3β is also a key regulator of the cellular components of both adaptive and innate immunity. As such, we sought to demonstrate the

(*Continued*.) hierarchical clustering. **B,** GSEA depicting significantly altered Hallmark (MSigDB) pathways after three cycles of complete combination therapy. **C,** Hierarchical clustering heatmap depicting overall gene expression patterns after treatment with complete combination therapy, marking short-term (red) and long-term (blue) clinical responses. **D,** Bar plot showing upregulated Hallmark pathways after GSEA of cluster 2 genes (enriched in nonresponders). **E,** EMT status by EMT-ISH staining, by patient, quantified via HALO-AI. Representative stained tumor histology images, with or without superimposed automated cell identification (right), are provided for each patient. Pie charts depicting the distribution of E vs. QM markers for each patient are shown. **F,** snRNA-seq UMAP of malignant cells from patients at cycle 12, with pie charts depicting the distribution of E vs. QM cell proportion for each patient shown to the right.

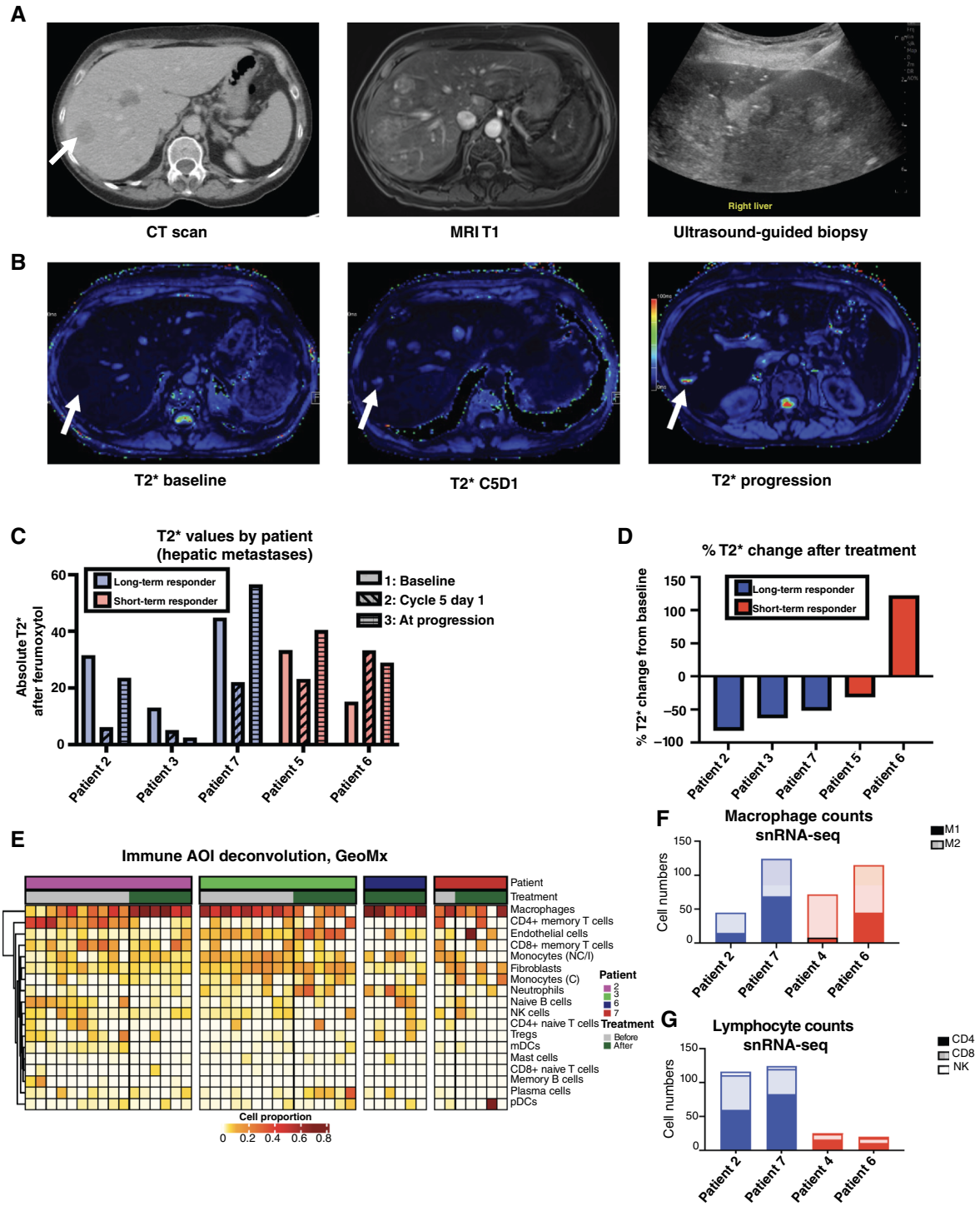

Figure 4.

Immune cell characterization of PDAC liver metastases by imaging, spatial transcriptomics, and snRNA-seq. Representative imaging from patient 2. **A,** Axial contrast-enhanced portal venous phase CT (left) prior to the initiation of therapy demonstrates multifocal hepatic metastases, including a lesion in the right lobe of the liver (arrow). The same lesion is seen on T1 after F-MRI imaging (middle) and was biopsied for tissue analysis by ultrasound guidance (right). **B,** T2* signal from F-MRI over time for this lesion with initial low values (represented as dark blue on color-compressed maps) and increasing T2* at cycle 5 day 1 and at progression (blue to green/red). Increasing T2* values suggest macrophage absence initially and subsequent recruitment at the metastatic disease sites. **C,** Quantification of absolute T2* signal in liver metastases in each patient over time. **D,** Percentage change of T2* from baseline to cycle 5 day 1. **E,** Proportion of tumor microenvironmental cell types using spatial transcriptomics immune AOI mixed cell deconvolution, by patient before and after treatment. Macrophages are the primary immune infiltrate in all samples. snRNA-seq of biopsies at cycle 12 of patients showing (**F**) M1 and M2 macrophage counts per sample and (**G**) CD4 T-cell, CD8 T-cell, and NK cell counts.

feasibility of utilizing integrated spatial transcriptomic analysis and snRNA-seq of serial tumor biopsies coordinated with F-MRI to clinically characterize TAM trafficking in a prospective interventional clinical trial. Our molecular analysis of biopsies from PDAC liver metastases revealed an immune microenvironment dominated by macrophages at 2 and 6 months of GSK-3β blockade. Interestingly, the prolonged exposure to ELRA over a 6-month period promoted M1 polarization of TAMs in long-term responders, whereas M2 TAMs predominated in the short-term responders. F-MRI T2* mapping demonstrated that tumor response to therapy was associated with an influx of macrophages. Conversely, the efflux of macrophages from patient tumors was associated with resistance to therapy. Thus, we demonstrate the feasibility of clinical monitoring of macrophage trafficking within patient tumors and the potential for understanding macrophage response to different therapeutic interventions. Similarly, snRNA-seq of biopsied tumors demonstrated the predominance of $CD4^+$ and $CD8^+$ tumor-infiltrating lymphocytes and NK cells in long-term responders. These findings, along with markers of clinical benefit such as a reduction in disease burden measured by RECIST and the prolonged time on MT with 5-FU in long-term responders, implicate the role of antitumor immunity associated with GSK-3β blockade via ELRA. In fact, Mahalingam and colleagues (23) observed the induction of $CD8^+$ tumor-infiltrating T cells in a subset of patients with a prolonged response to ELRA, gemcitabine, and nab-paclitaxel in the randomized phase II study. Together, these data support a model in which GSK-3β blockade with ELRA modulates the function of cellular components of adaptive and innate immunity to facilitate a tumor-suppressive immune microenvironment.

In summary, our findings in this limited patient population support the hypothesis that leveraging GSK-3β blockade to target alterations in PDAC plasticity associated with chemotherapy exposure offers a unique strategy to pharmacologically induce synthetic lethality with FOLFIRINOX. Simultaneously, GSK-3β blockade may modulate immune cell function to develop a tumor-suppressive microenvironment. NCT05077800 has now completed patient enrollment, and its multiarm design will allow for the determination of the relative contributions of ELRA and LOS to FOLFIRINOX sensitivity in patients with metastatic PDAC.

Data Availability

RNA-seq data and NanoString GeoMx are available at NCBI Gene Expression Omnibus, GSE311574 study. Please contact D.T. Ting for raw data inquiries.

Authors' Disclosures

E.W. Lin reports grants from the National Institute of Diabetes and Digestive and Kidney Diseases during the conduct of the study. A. O'Shea reports other support from Novartis during the conduct of the study. L.S. Blaszkowsky reports ownership of stock in Pfizer. A.R. Parikh reports ownership of equity in C2i Genomics, Khora, OneCell, XGenomes, Cadex, and Parithera and that in the past 36 months, A.R. Parikh has served as an advisor/consultant for Zola, CVS, Phesi, Xilio, 3T Biosciences, Do More Diagnostics, Summit Therapeutics, Pfizer, Regeneron, GSK, Foundation Medicine, Careset, Value Analytics Labs, Naterara, Adroya, AstraZeneca, Scare, Hookipa, Guardant, AbbVie, Seagen, Mirati, Takeda, PMV, Kahr, Sirtex, Eli Lilly, Merck, Amgen, Delicate, Exact, Caris, Bristol Myers Squibb, Incyte, Pheon, Neogenomics, J & J, Exact Third Rock Ventures, MPM Capital, and Science For America; is chief scientist of Reversing Early Recurrence; receives fees from UptoDate; has received travel fees from Karkinos Healthcare; and has received research funding to the institution from PMV Pharmaceuticals, Bristol Myers Squibb, Mirati, Erasca, Genentech, Daiichi Sankyo, Syndax, Revolution Medicine, Lilly, Xilio, and Parthenon. R. Uppot reports other support from Boston Scientific outside the submitted work. D.T. Ting reports personal fees and other support from ROME Therapeutics and PanTher Therapeutics; other support from TellBio Inc., ImproveBio Inc., and 65 Therapeutics; grants and personal fees from Astellas; grants from Sanofi and Incyte; and personal fees from AstraZeneca, Leica Biosystems, abrdn, Moderna, and Sonata Therapeutics outside the submitted work. C.D. Weekes reports grants from Actuate Therapeutics during the conduct of the study; personal fees from Actuate Therapeutics outside the submitted work; consulting fees from PanTher Therapeutics, Actuate Therapeutics, Novartis, Genentech, and Merck Pharmaceuticals; and membership on the scientific advisory board with equity for VRise Therapeutics and Cymon Bio, Inc., which are not related to this work; in addition, C.D. Weekes receives research support from Novartis, Genentech, Elicio Therapeutics, Deciphera, and Actuate Therapeutics. C.D. Weekes's interests were reviewed and are managed by Mass General Brigham in accordance with their conflict of interest policies. No disclosures were reported by the other authors.

Authors' Contributions

E.W. Lin: Conceptualization, resources, data curation, formal analysis, supervision, funding acquisition, validation, investigation, visualization, methodology, writing–original draft, project administration, writing–review and editing. **P. Pathak:** Conceptualization, resources, data curation, formal analysis, supervision, visualization, methodology, writing–original draft, writing–review and editing. **A. O'Shea:** Conceptualization, resources, data curation, formal analysis, supervision, visualization, writing–original draft, writing–review and editing. **B. Awasthi:** Conceptualization, resources, data curation, formal analysis, supervision, investigation, visualization, methodology, writing–original draft, writing–review and editing. **I.E. Phillips:** Formal analysis, investigation. **J.R. Kocher:** Investigation. **Y. Song:** Formal analysis, investigation, methodology. **M.J. Raabe:** Formal analysis, investigation. **K.H. Xu:** Formal analysis, investigation, visualization, methodology. **B.K. Patel:** Investigation. **N. Lester:** Investigation. **J.W. Bae:** Investigation. **M.L. Zhang:** Investigation. **L.T. Nieman:** Resources, formal analysis, visualization, methodology, project administration. **L.S. Blaszkowsky:** Resources. **E.P. Walsh:** Resources. **A.R. Parikh:** Resources. **A. Hansen:** Resources. **J. Caufield:** Resources. **G. Newbert:** Resources. **A.W. Asombang:** Resources. **B. Casey:** Resources. **J. Cohen:** Resources. **B.C. Jacobson:** Resources. **K. Krishnan:** Resources. **R. Uppot:** Resources. **R. Weissleder:** Resources. **N.K. Horick:** Formal analysis, visualization. **W.L. Hwang:** Conceptualization, resources, data curation, software, formal analysis, supervision, validation, investigation, visualization, methodology, writing–original draft, project administration, writing–review and editing. **M.G. Harisinghani:** Conceptualization, resources, data curation, software, formal analysis, supervision, validation, investigation, visualization, methodology, writing–original draft, project administration, writing–review and editing. **D.T. Ting:** Conceptualization, resources, data curation, software, formal analysis, supervision, funding acquisition, validation, investigation, visualization, writing–original draft, project administration, writing–review and editing. **C.D. Weekes:** Conceptualization, resources, data curation, formal analysis, supervision, funding acquisition, validation, investigation, visualization, methodology, writing–original draft, project administration, writing–review and editing.

Acknowledgments

We are grateful to Danielle Bestoso and Angelique Gilbert for their administrative support. Additionally, we would like to acknowledge the Program for Coordination of Research Protocols in the Massachusetts General Hospital Cancer Center Protocol Office for the multicenter coordination and monitoring of the trial. Funding support was received from ACD-Biotechne (D.T. Ting), Zebunisha Juma Endowed Chair (D.T. Ting), Massachusetts Life Sciences Center Research Infrastructure Program (D.T. Ting), Christopher D. Horner Endowed Chair (C.D. Weekes), Dr. Robert F. Vizza Lustgarten Clinical Accelerator Initiative (C.D. Weekes), and Actuate Therapeutics, Inc. (C.D. Weekes).

Note

Supplementary data for this article are available at Clinical Cancer Research Online (http://clincancerres.aacrjournals.org/).

Received May 31, 2025; revised August 9, 2025; accepted December 4, 2025; posted first December 9, 2025.

References

1. Conroy T, Desseigne F, Ychou M, Bouché O, Guimbaud R, Bécouarn Y, et al. FOLFIRINOX versus gemcitabine for metastatic pancreatic cancer. N Engl J Med 2011;364:1817–25.
2. Von Hoff DD, Ervin T, Arena FP, Chiorean EG, Infante J, Moore M, et al. Increased survival in pancreatic cancer with nab-paclitaxel plus gemcitabine. N Engl J Med 2013;369:1691–703.
3. Moffitt RA, Marayati R, Flate EL, Volmar KE, Loeza SG, Hoadley KA, et al. Virtual microdissection identifies distinct tumor- and stroma-specific subtypes of pancreatic ductal adenocarcinoma. Nat Genet 2015;47:1168–78.
4. Bailey P, Chang DK, Nones K, Johns AL, Patch AM, Gingras MC, et al. Genomic analyses identify molecular subtypes of pancreatic cancer. Nature 2016;531:47–52.
5. Tiriac H, Belleau P, Engle DD, Plenker D, Deschênes A, Somerville TDD, et al. Organoid profiling identifies common responders to chemotherapy in pancreatic cancer. Cancer Discov 2018;8:1112–29.
6. Collisson EA, Bailey P, Chang DK, Biankin AV. Molecular subtypes of pancreatic cancer. Nat Rev Gastroenterol Hepatol 2019;16:207–20.
7. Aung KL, Fischer SE, Denroche RE, Jang GH, Dodd A, Creighton S, et al. Genomics-driven precision medicine for advanced pancreatic cancer: early results from the COMPASS trial. Clin Cancer Res 2018;24:1344–54.
8. O'Kane GM, Grünwald BT, Jang GH, Masoomian M, Picardo S, Grant RC, et al. GATA6 expression distinguishes classical and basal-like subtypes in advanced pancreatic cancer. Clin Cancer Res 2020;26:4901–10.
9. Ligorio M, Sil S, Malagon-Lopez J, Nieman LT, Misale S, Di Pilato M, et al. Stromal microenvironment shapes the intratumoral architecture of pancreatic cancer. Cell 2019;178:160–75.
10. Porter RL, Magnus NKC, Thapar V, Morris R, Szabolcs A, Neyaz A, et al. Epithelial to mesenchymal plasticity and differential response to therapies in pancreatic ductal adenocarcinoma. Proc Natl Acad Sci U S A 2019;116:26835–45.
11. Huang W, Navarro-Serer B, Jeong YJ, Chianchiano P, Xia L, Luchini C, et al. Pattern of invasion in human pancreatic cancer organoids is associated with loss of SMAD4 and clinical outcome. Cancer Res 2020;80:2804–17.
12. Chan-Seng-Yue M, Kim JC, Wilson GW, Ng K, Figueroa EF, O'Kane GM, et al. Transcription phenotypes of pancreatic cancer are driven by genomic events during tumor evolution. Nat Genet 2020;52:231–40.
13. Raghavan S, Winter PS, Navia AW, Williams HL, DenAdel A, Lowder KE, et al. Microenvironment drives cell state, plasticity, and drug response in pancreatic cancer. Cell 2021;184:6119–37.e26.
14. Rhim AD, Mirek ET, Aiello NM, Maitra A, Bailey JM, McAllister F, et al. EMT and dissemination precede pancreatic tumor formation. Cell 2012;148:349–61.
15. Aiello NM, Maddipati R, Norgard RJ, Balli D, Li J, Yuan S, et al. EMT subtype influences epithelial plasticity and mode of cell migration. Dev Cell 2018;45:681–95.e4.
16. Brunton H, Caligiuri G, Cunningham R, Upstill-Goddard R, Bailey UM, Garner IM, et al. HNF4A and GATA6 loss reveals therapeutically actionable subtypes in pancreatic cancer. Cell Rep 2020;31:107625.
17. Shimasaki T, Kitano A, Motoo Y, Minamoto T. Aberrant glycogen synthase kinase 3β in the development of pancreatic cancer. J Carcinog 2012;11:15.
18. Ougolkov AV, Fernandez-Zapico ME, Bilim VN, Smyrk TC, Chari ST, Billadeau DD. Aberrant nuclear accumulation of glycogen synthase kinase-3beta in human pancreatic cancer: association with kinase activity and tumor dedifferentiation. Clin Cancer Res 2006;12:5074–81.
19. Chauhan VP, Martin JD, Liu H, Lacorre DA, Jain SR, Kozin SV, et al. Angiotensin inhibition enhances drug delivery and potentiates chemotherapy by decompressing tumour blood vessels. Nat Commun 2013;4:2516.
20. Murphy JE, Wo JY, Ryan DP, Clark JW, Jiang W, Yeap BY, et al. Total neoadjuvant therapy with FOLFIRINOX in combination with losartan followed by chemoradiotherapy for locally advanced pancreatic cancer: a phase 2 clinical trial. JAMA Oncol 2019;5:1020–7.
21. Ougolkov AV, Fernandez-Zapico ME, Savoy DN, Urrutia RA, Billadeau DD. Glycogen synthase kinase-3beta participates in nuclear factor kappaB-mediated gene transcription and cell survival in pancreatic cancer cells. Cancer Res 2005;65:2076–81.
22. Ding L, Madamsetty VS, Kiers S, Alekhina O, Ugolkov A, Dube J, et al. Glycogen synthase kinase-3 inhibition sensitizes pancreatic cancer cells to chemotherapy by abrogating the TopBP1/ATR-mediated DNA damage response. Clin Cancer Res 2019;25:6452–62.
23. Mahalingam D, Shroff RT, Carneiro BA, Ji Y, Coveler AL, Cervantes A, et al Preliminary results from the randomized phase 2 study (1801 part 3B) of elraglusib in combination with gemcitabine/nab-paclitaxel (GnP) versus GnP alone in patients (pts) with previously untreated metastatic pancreatic ductal adenocarcinoma (mPDAC). J Clin Oncol 2025;43::4006.
24. Zheng S, Wang W, Aldahdooh J, Malyutina A, Shadbahr T, Tanoli Z, et al. SynergyFinder plus: toward better interpretation and annotation of drug combination screening datasets. Genomics Proteomics Bioinformatics 2022;20:587–96.
25. Hwang WL, Jagadeesh KA, Guo JA, Hoffman HI, Yadollahpour P, Reeves JW, et al. Single-nucleus and spatial transcriptome profiling of pancreatic cancer identifies multicellular dynamics associated with neoadjuvant treatment. Nat Genet 2022;54:1178–91.
26. Azizi E, Carr AJ, Plitas G, Cornish AE, Konopacki C, Prabhakaran S, et al. Single-cell map of diverse immune phenotypes in the breast tumor microenvironment. Cell 2018;174:1293–308.e36.
27. Andreatta M, Corria-Osorio J, Müller S, Cubas R, Coukos G, Carmona SJ. Interpretation of T cell states from single-cell transcriptomics data using reference atlases. Nat Commun 2021;12:2965.
28. Ding J, Smith SL, Orozco G, Barton A, Eyre S, Martin P. Characterisation of CD4+ T-cell subtypes using single cell RNA sequencing and the impact of cell number and sequencing depth. Sci Rep 2020;10:19825.
29. Xue Z, Wu L, Tian R, Gao B, Zhao Y, He B, et al. Integrative mapping of human CD8+ T cells in inflammation and cancer. Nat Methods 2025;22:435–45.
30. McLaughlin RA, Jonker DJ, Karanicolas PJ, Ko Y-J, Welch S, Renouf DJ, et al. NeoPancONE: GATA6 expression as a predictor of benefit to perioperative modified FOLFIRINOX in resectable pancreatic adenocarcinoma (r-PDAC): a multicentre phase II study. J Clin Oncol 2025;43(suppl):4011.
31. Corcoran RB, Contino G, Deshpande V, Tzatsos A, Conrad C, Benes CH, et al. STAT3 plays a critical role in KRAS-induced pancreatic tumorigenesis. Cancer Res 2011;71:5020–9.
32. Aghighi M, Theruvath AJ, Pareek A, Pisani LL, Alford R, Muehe AM, et al. Magnetic resonance imaging of tumor-associated macrophages: clinical translation. Clin Cancer Res 2018;24:4110–8.
33. Knox JJ, Jaffee EM, O'Kane GM, King D, Laheru D, Yu KH, et al. Early results of the PASS-01 trial: pancreatic adenocarcinoma signature stratification for treatment-01. J Clin Oncol 2024;42(suppl):LBA4004.
34. Maier HJ, Schmidt-Strassburger U, Huber MA, Wiedemann EM, Beug H, Wirth T. NF-kappaB promotes epithelial-mesenchymal transition, migration and invasion of pancreatic carcinoma cells. Cancer Lett 2010;295:214–28.